RESEARCH ARTICLE

Insights from a new method providing single-shot, planar measurement of gas-phase temperature in particle-laden flows under high-flux radiation

Elliott W. Lewis[1,3] · Timothy C. W. Lau[3,4] · Zhiwei Sun[1,3] · Zeyad T. Alwahabi[2,3] · Graham J. Nathan[1,3]

Abstract

Two-colour laser-induced fluorescence (LIF) of toluene has been demonstrated to provide in situ, spatially resolved, planar measurements of the gas-phase temperature in a particle-laden flow with strong radiative heating at fluxes up to 42.8 MW/m^2. Toluene was seeded in trace quantities into the gas flow laden with particles of mean diameter 173 µm at a volumetric loading sufficiently high for particle–fluid and particle–particle interactions to be significant. The particle number density was also measured simultaneously using Mie scattering. The two-colour LIF method was found to resolve temperature with a pixel-to-pixel standard deviation of 17.8 °C for unheated measurements in this system despite significant attenuation of the probe laser and signal trapping of the fluorescence emissions from the densely loaded particles. Following heating of the particles using high flux radiation, the increase in the gas-phase temperature from convection was found to be spatially non-uniform with highly localised regions of temperature spanning from ambient to 150 °C. This gas-phase heating continued well downstream from the limits of the region with radiative heating, with the time-averaged gas temperature increasing with distance at up to 2,200 °C/m on the jet centreline. The temperature of the flow was non-symmetrical in the direction of the heating beam, because the particles attenuate the radiation through absorption and scattering. The addition of radiation at fluxes up to 42.8 MW/m^2 did not significantly change the particle number density distribution within the region investigated here.

Graphic abstract
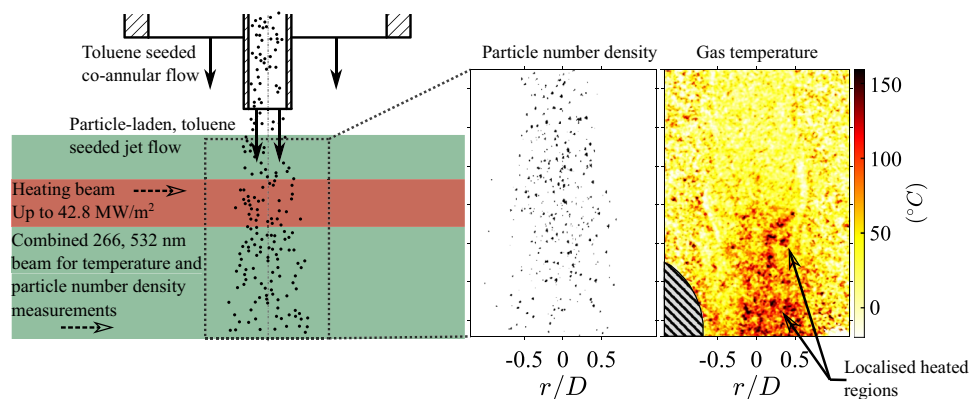
1 Introduction

Particle-laden flows with strong radiative heat transfer are present in a range of systems including particle-based concentrated solar thermal (CST) receivers, flash calciners for alumina and cement production, and combustion of

✉ Elliott W. Lewis
   elliott.lewis@adelaide.edu.au

Extended author information available on the last page of the article

particulate fuels. The particles in these systems are typically heated rapidly following the absorption of high-flux radiation from a flame, concentrated sunlight, or from a chemical reaction such as combustion. The resulting strong thermal gradients lead to complex and nonlinear heat transfer from both convective and radiative processes between the heat source, particles, fluid and the surroundings (Miller and Koenigsdorff 1991; Watanabe et al. 2008). These processes are further complicated by nonlinear and mutually interacting phenomena in particle-laden flows such as turbulence, particle clustering (Lau et al. 2019), and particle–fluid coupling (Elgobashi 2006). These phenomena can affect the mean and instantaneous velocity and particle number density distributions (Lau and Nathan 2014), which in turn affect both the radiative and convective heat transfer. Detailed understanding of these complex, coupled phenomena requires accurate, spatially resolved, multi-dimensional and simultaneous measurements of the temperature and velocity of both phases, together with the local particle concentration (number density). However, such measurements of all of these parameters are not presently available, partially due to the challenging experimental arrangement required and lack of suitable techniques. Recent experiments have begun to address this gap (Abram et al. 2017; Jainski et al. 2014; Kueh et al. 2017). However, there are currently no reports of in situ and well-resolved measurements of the gas-phase temperature in particle-laden flows with strong radiative heating.

Previous numerical models of particles heated with high-flux radiation in particle receivers have shown that heat transfer between the radiation source and the particles, together with that between the particles and fluid, is strongly dependent on both the particle size and number density (Chen et al. 2006; Evans et al. 1987). Furthermore, it has been demonstrated that particle clustering, whereby particles are preferentially concentrated in highly localised regions, impacts heat transfer processes and local temperature distributions (Pouransari and Mani 2016), which in turn affect the efficiency of the system. Additionally, the heating of particles in suspension by radiation at sufficiently high fluxes can induce turbulence in the flow (Zamansky et al. 2014) and reduce the particle settling velocity (Frankel et al. 2016) from the generation of buoyant plumes around the heated particles. The complexity of particle–fluid interactions in these systems also increases with particle volumetric loading ($\phi = \dot{V}_p / \dot{V}_f$, where $\dot{V}_p$ and $\dot{V}_f$ are the volumetric flow rates of the particles and fluid, respectively). Additional particle–gas interactions occur for flows in the two-way coupling regime (for $10^{-6} < \phi < 10^{-3}$), and particle–particle interactions also occur in the four-way coupling regime (for $\phi > 10^{-3}$), as defined by Elgobashi (2006). These mutually interacting, complex phenomena result in particle-laden flows being difficult to model reliably without both new understanding

and computationally expensive direct numerical simulations. Therefore, detailed experimental measurements of both the flow temperature and particle concentration are required to enable the development and validation of reliable, simplified models of these flows.

The use of experimental techniques with high spatial and temporal resolution in multiple dimensions is needed to provide measurements of spatial and temporal gradients in turbulent flows. Laser-based techniques are a suitable choice, as these have the potential to provide spatially resolved two-dimensional measurements from a nanosecond scale laser pulse. However, utilising laser-based methods in particle-laden flows is difficult due to the challenges of laser attenuation, signal trapping (Kalt et al. 2007), multiple scattering (Berrocal et al. 2008), and particle luminescence (Lewis et al. 2020). These challenges are particularly significant in flows with the high particle loadings ($\phi > 10^{-3}$) that are used in most practical systems, resulting in a paucity of detailed experimental measurements in such environments. Previous thermometry measurements of particle-laden flows with radiative heating include point measurements of the gas and walls using thermocouples in a CST particle receiver (Siegel et al. 2010), a vortex particle receiver (Davis et al. 2017) and square duct (Banko et al. 2020), as well as planar particle temperature measurements in a jet (Kueh et al. 2018). However, there are currently no in situ planar measurements of the gas temperature in densely loaded particle-laden flows heated by high-flux radiation that are spatially and temporally resolved. As such there is a need for experimental measurements of parameters including gas temperature to improve the current understanding of these flows.

Several techniques have been implemented to measure the instantaneous, planar gas temperature in a variety of flows, including laser Rayleigh scattering (LRS) (Miles et al. 2001), laser-induced phosphorescence (LIP) (Abram et al. 2017) and laser-induced fluorescence (LIF) (Schulz and Sick 2005). In LRS, the thermometry signal is at the same wavelength as the excitation source (i.e. the laser), which results in significant interference from Mie scattering in flows with particles. Filtered LRS is a technique that has been used to suppress scattered laser light and stray light from other sources. However, the Mie scattering from particles is several orders of magnitude stronger than the Rayleigh signal leading to difficulties isolating the Rayleigh signal from the Mie scattering. Additionally, the LRS signal is proportional to the local laser flux, which is highly non-uniform in a densely loaded particle-laden flow due to attenuation and multiple scattering. The LIF and LIP methods both have thermometry signals that are separable from scattered light using optical filtering and thus are well suited for measurements in particle-laden flows. However, LIP for gas-phase thermometry typically utilises small tracer particles in the flow together with the assumption that the two phases are

in thermal equilibrium. In a flow subject to high-flux radiation, this assumption does not hold because of absorption of the high-flux radiation by the particles, which results in a temperature difference between the particles and gas. In contrast, LIF thermometry typically utilises gas tracers that give a direct measurement of the gas-phase temperature. While LIF thermometry is a mature technique, its accuracy particle-laden flows has only begun to be assessed recently in an isothermal flow (Lewis et al. 2020). LIF thermometry has yet to be applied to measure gas-phase temperatures with high spatial resolution in industrially relevant particle-laden flows with strong thermal gradients.

Therefore, the objective of the present investigation is to determine the spatially resolved gas-phase temperature distribution in a particle-laden flow with a volumetric loading sufficiently high to be in the four-way coupling regime and with high-flux radiative heating. This measurement is a step towards improving understanding of heat transfer in particle-laden flows, in particular particle-laden flows with significant particle–fluid and particle–particle interactions. More specifically, we aim to experimentally determine the mean and instantaneous gas-phase temperature distributions in a well-characterised particle-laden flow heated at a systematically varied series of radiative fluxes up to 42.8 MW/m^2. We also aim to provide some new insights from these measurements.

2 Methodology

2.1 Two-colour LIF thermometry

Toluene was chosen as the fluorescing species for LIF thermometry measurements because it has been previously demonstrated in flows with a range of challenging conditions including in a particle-laden jet (Lewis et al. 2020), in flows with droplets (Jainski et al. 2014; Tea et al. 2011), near to surfaces at kHz rates (Cundy et al. 2011) and in shock tubes (Miller et al. 2013). Toluene is a well-characterised fluorescent tracer suitable for measurements at temperatures of $280\,\text{K} < T_g < 600\,\text{K}$ with an emission spectrum that is highly sensitive to temperature (Faust et al. 2014). Toluene LIF thermometry using the two-colour ratio method utilises the shift of the emission spectrum to longer wavelengths with increasing temperature (Koban et al. 2004). The intensity of fluorescence emissions (I) at each wavelength (λ) after excitation by a suitable light source is dependent on the local toluene concentration (n), laser pulse energy (Q_{laser}), the absorption cross section (σ_{abs}) and fluorescence quantum yield (Φ_F). Importantly, both σ_{abs} and Φ_F, and subsequently the absorption and fluorescence emission, of toluene are temperature (T) dependent (Schulz and Sick 2005). The spatially resolved emission intensity of a dispersed fluorescent

tracer in a flow, following excitation at a single wavelength using a laser formed into a sheet, is described by the following equation:

$$I_\lambda \propto Q_{laser}(x,r)n(x,r)\sigma_{abs}(T(x,r))\Phi_{F,\lambda}(T(x,r)) \tag{1}$$

where x and r are two relevant spatial coordinates of the flow. The influence of the spatially dependent parameters can be removed by taking the ratio of emissions in two spectral bands formed using optical filtering. The resultant ratio of signals measured by two cameras aligned to view along the same optical path through the flow, each measuring the intensity of fluorescence emissions in a filtered spectral band (S_λ), is shown to reduce to a function of temperature only by the equation:

$$\frac{S_{\lambda1}}{S_{\lambda2}} = \frac{\eta_{\lambda1}\Phi_{F,\lambda1}(T)}{\eta_{\lambda2}\Phi_{F,\lambda2}(T)} = f(T) \tag{2}$$

where η is the camera collection efficiency at the filtered wavelengths and f is a function that can be determined through calibration. Importantly, the intensity ratio is not dependent on the local laser fluence, Q_{laser}, or the toluene concentration, n, removing the necessity to correct the measured fluorescence emission for laser sheet attenuation, beam profile and mixing of the toluene seeded flow with the ambient gas.

2.2 Experimental arrangement

The experiment consisted of a system to provide simultaneous gas-phase thermometry and particle number density measurements in a particle-laden flow heated with high-flux radiation, as presented in Fig. 1. The central flow issues from a long pipe with diameter $D = 12.6$ mm to generate a jet, with a development length of $165D$ that is sufficiently long to approach a fully developed particle-laden pipe flow (Lau and Nathan 2014). The central pipe is aligned within a co-annular pipe of diameter 69 mm, which is used to generate a co-flow. The coordinate systems for the flow and optical system, together with the size of the measurement region, are presented in Fig. 2. The jet pipe was positioned centrally within a vertically oriented, downward directed wind tunnel of 300 mm square cross section. This arrangement was designed such that the pipe jet matches that investigated by Lau and Nathan (2016). The central pipe had a bulk velocity of $U_{g,b} = 3.6$ m/s, which was chosen because it was the lowest velocity at which the particles were effectively carried by the flow. A low velocity was desired to increase the residence time, and therefore the temperature rise, of the particles in the heating region. The resultant Reynolds number of the jet is $Re_D = \frac{\rho U_{g,b} D}{\mu} = 3000$, where ρ and μ are the density and dynamic viscosity of the flow, respectively. The velocity of the annular co-flow and wind tunnel co-flow were
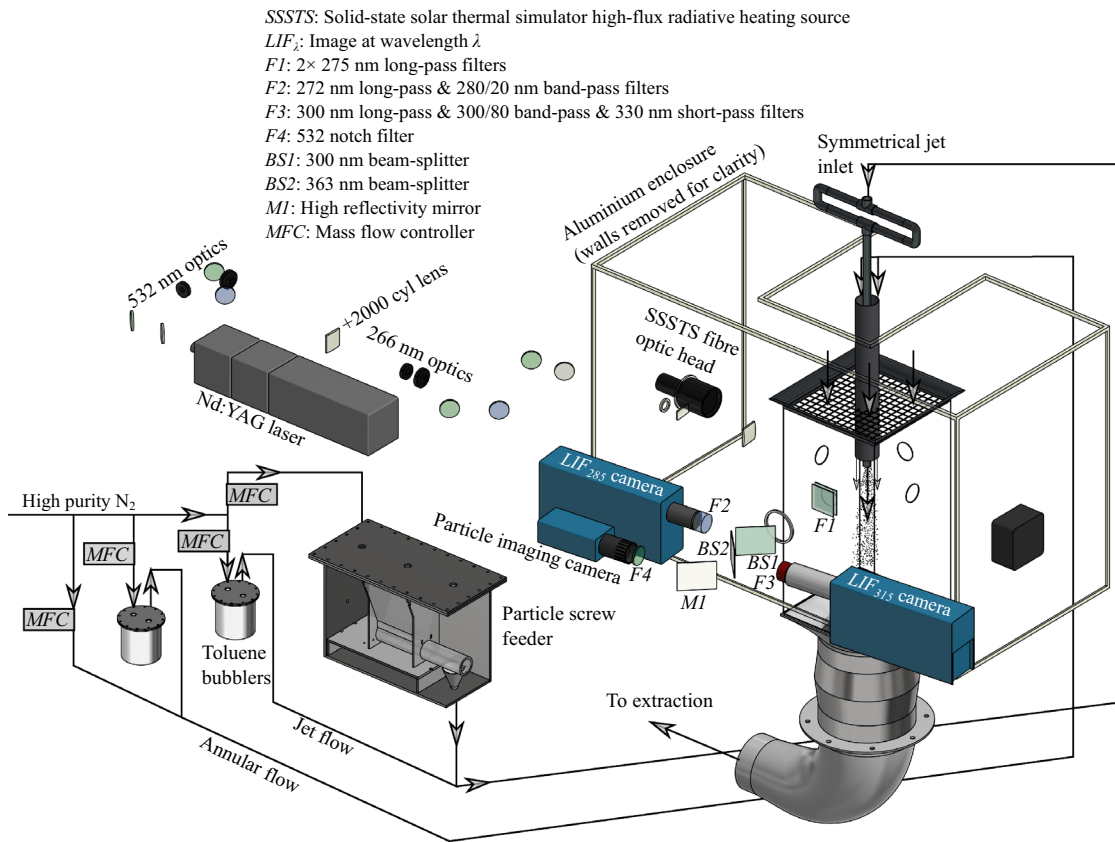
SSSTS: Solid-state solar thermal simulator high-flux radiative heating source
LIF$_\lambda$: Image at wavelength λ
F1: 2× 275 nm long-pass filters
F2: 272 nm long-pass & 280/20 nm band-pass filters
F3: 300 nm long-pass & 300/80 nm band-pass & 330 nm short-pass filters
F4: 532 notch filter
BS1: 300 nm beam-splitter
BS2: 363 nm beam-splitter
M1: High reflectivity mirror
MFC: Mass flow controller

Fig. 1 Experimental arrangement for simultaneous two-colour LIF thermometry and particle number density measurements of a particle-laden flow heated with high-flux radiation
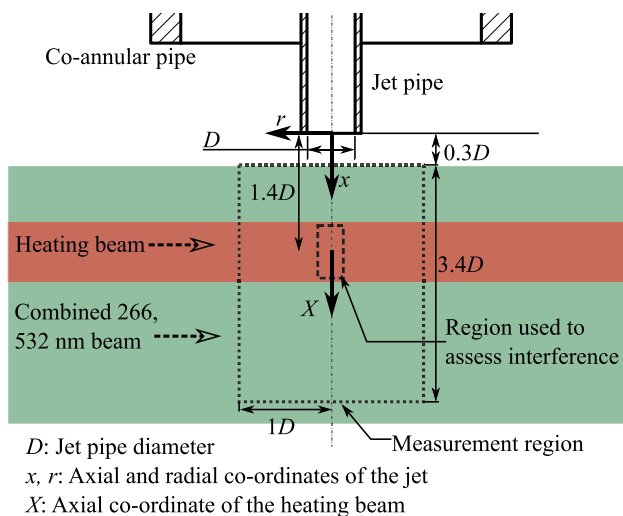

Fig. 2 Schematic diagram of the region of interest showing key dimensions and the coordinate system (not to scale)

both less than 0.5 m/s. Both the jet and annular flows employed high purity nitrogen as the carrier gas. Toluene and particles were seeded separately into two streams and then combined to form the jet flow, with the particles introduced into one stream with a volumetric flow rate of 18 SLPM using a screw feeder in a sealed container. The second stream, with a volumetric flow rate of 7 SLPM, was bubbled through liquid toluene held at ambient temperature, resulting in a toluene concentration of approximately 0.75% by volume for the combined jet flow. This concentration was estimated using the assumption that the outlet flow from the toluene bubbler is saturated. For the annular flow a 50 SLPM stream of nitrogen was combined with a toluene seeded stream of 5 SLPM, with a resultant toluene concentration in the annular flow of approximately 0.25% by volume. The toluene concentration in the annulus differed from that of the jet to allow for clear identification of the jet edges. The volumetric flow rates of each of these four flows were controlled by separate mass flow controllers (MFCs). Nitrogen was used as the carrier gas for both the jet and annular flow because the presence of oxygen strongly quenches the fluorescence emissions from toluene (Koban et al. 2005).

Aluminosilicate ceramic (Carbobead CP 70/140) particles with an absolute density of 3.27 g/cm^3 and an average sphericity of 0.9 were seeded in the jet flow using a screw feeder. The time-averaged volumetric loading of particles was

chosen to be $\bar{\phi} = 1.4 \times 10^{-3}$, resulting in a particle-laden flow within the four-way coupling regime. The physical design of a screw feeder introduces a sinusoidal variation in the particle loading with time, which is particularly significant at low screw speeds. This effect was reduced using a screw with 4 flights operating at rotational speeds > 30 rpm. The resultant standard deviation in particle loading with time was 14.8% of the time-averaged mean. The particle diameter (d_p) distribution of the Carbobead CP 70/140 particles, as measured using a Malvern Mastersizer 2000, is presented in Fig. 3. The measured mean diameter by volume was $d_p = 173$ μm, with 80% of particles in the range of $125 < d_p < 235$ μm. The resultant particle Stokes number, which is the ratio of the particle to flow time response (Eaton and Fessler 1994), for the large-scale motions in the jet was

$$Sk_D = \frac{\rho_p \bar{d}_p^2 U_{g,b}}{18\mu D} = 77.$$

2.3 Optical arrangement

A Quantel Q-smart laser operating at 10 Hz with two frequency doublers was used to generate second- and fourth-harmonic beams with respective wavelengths of 532 nm and 266 nm. Both beams were formed into co-planar sheets 60 mm high and approximately 0.6 mm thick in the measurement region of $|r/D| < 2$ and $0.3 < x/D < 3.7$, where x and r are the respective axial and radial coordinates of the jet. The combined laser sheet was aligned to pass through the jet centreline, as can be seen from Fig. 1. The pulse energies of each wavelength, controlled using separate wave-plates and polarisers, were 18 and 0.5 mJ/pulse for the 266 and 532 nm beams, respectively. The resultant fluences in the measurement region of the laser sheets were 50 and 1.4 mJ/cm^2, respectively. The radiative heating source was a solid-state solar thermal simulator (SSSTS), which is a diode laser bundle with a fibre optic head emitting a collimated,
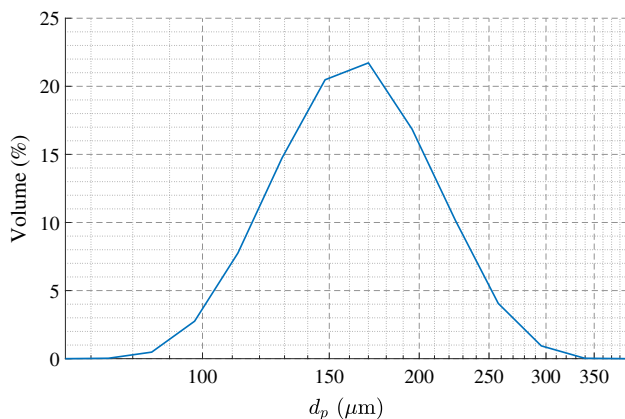
monochromatic infra-red (910 nm) beam with a full-width half maximum diameter of 7.34 mm as described by Alwahabi et al. (2016). The SSSTS beam was centred on the jet centreline 17.5 mm downstream from the jet exit plane. The intensity profile of the SSSTS beam, I, on the jet centreline, normalised by the peak intensity I_{peak}, is presented in Fig. 4. Here X is the coordinate of the SSSTS beam co-linear with x, with the origin situated at the intersection of the SSSTS beam centre and the jet centreline. This profile was measured by imaging the reflection of the SSSTS beam from a diffuse glass plate angled at 45° to the beam direction. The SSSTS beam was absorbed by a water-cooled power meter (Gentec model HP100A-4KWHE) that measured the instantaneous SSSTS power at 10 Hz, located in the path of the beam after passing through the wind tunnel. For safety, the SSSTS fibre optic head, power meter and wind tunnel were all positioned inside an interlocked brick-lined aluminium enclosure during operation. During the experiments the flux of the SSSTS beam was varied in the range of $0 < \dot{Q}''_{peak} < 42.8$ MW/m^2, where $\dot{Q}''_{peak}$ is the peak heating flux of the SSSTS calculated using time-averaged power measured with the power meter and the profile in Fig. 4.

Optical filtering was firstly used to separate the fluorescence emissions of the toluene (which are in the spectral region of 270–340 nm) from the elastically scattered light at 266 and 532 nm, and secondly used to separate the fluorescence emissions into two spectral bands centred at 285 and 315 nm (S_{285} and S_{315}, respectively). To achieve this, the scattered and emitted light was initially passed through two 275 nm long-pass filters (Asahi Spectra ZUL0275), each with an optical density of 2.5 at 266 nm, to suppress
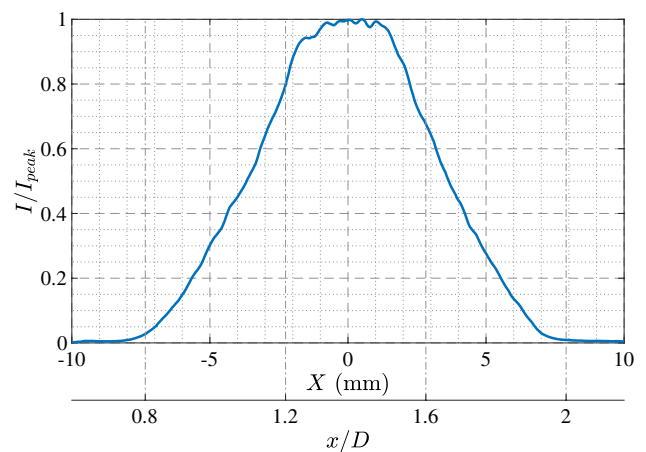

Fig. 3 The measured size distribution for the Carbobead CP 70/140 particles

Fig. 4 Solid-state solar thermal simulator (SSSTS) intensity profile normalised by the peak intensity, measured on the jet centreline in the axial direction. The profile is presented for the axial coordinate of both the jet flow (x) and heating beam X), which are described in Fig. 2

the majority of elastically scattered 266 nm laser light. Two dichroic beam-splitters (Semrock FF310-Di01, Di01-R355) were then used to separate S_{285} and S_{315} from the Mie scattered light at 532 nm. The fluorescence channels S_{285} and S_{315} were then refined using a series of optical filters and captured using two separate PCO Di-Cam intensified s-CMOS camera. The S_{285} channel was formed using a 272 nm long-pass (Semrock FF01-272LP) and 280 nm band-pass filter (Semrock BP280/20), with the resultant transmission band of 285 ± 5 nm being focussed using a spherical UV lens ($f = 100$ mm, Thorlabs LB4821). The S_{315} channel was formed using a 300 nm long-pass (Semrock FF01-300/LP), 330 nm short-pass (Semrock FF01-330/SP) and a 300 nm band-pass filter (Semrock FF01-300/80), with a resultant transmission band of 315 ± 10 nm being focussed using a Sodern UV 100 mm F/2.8 lens. The transmission efficiency of each channel is presented in Fig. 5, and the filter combinations are summarised in Table 1. These filter combinations were chosen to form the two-colour fluorescence bands at 285 ± 5 nm and 315 ± 10 nm because a strong signal is expected for both these bands, and because the resultant two-colour ratio is sensitive to changes in temperature within the gas temperature (T_g) ranges expected in
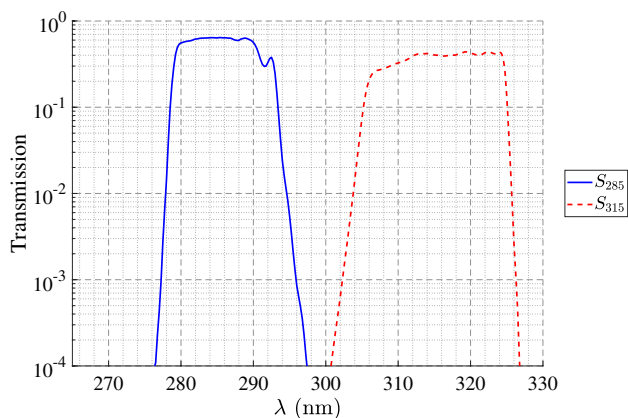
the current experiments of $20\,°C < T_g < 200\,°C$ (Miller et al. 2013). The filters used to form both of the channels used for two-colour LIF also effectively suppress elastically scattered laser light at 266 nm, 532 nm and 910 nm, with a calculated optical density > 6 at these wavelengths.

The particles were imaged using the Mie scattering from the 532 nm laser that was transmitted through the two beam-splitters described earlier. The scattered light was then reflected by a mirror (Thorlabs PFSQ20-03-F01) and filtered using a 532 nm notch filter to form the particle detection channel (S_{532}). This channel was imaged using a PCO.2000 CCD with a Tamron macro 80–210 mm lens.

Each of the three cameras had a gate width of 1 μs that opened approximately 100 ns before the laser pulse, with images recorded at the laser pulse frequency of 10 Hz. The spatial resolution for S_{285}, S_{315} and S_{532} was 17.8, 15.5 and 27.3 px/mm, respectively. The resolution for the two fluorescence cameras was matched as closely as possible within the limitations of the available space and lenses. The three cameras were located on the same side of the wind tunnel so that all attenuation and signal trapping effects interfering with the signal were the same for each camera.

The Carbobead ceramic particles used here were found, from measurements using a spectrometer (Princeton Instruments Acton Series Spectrograph), to have no significant luminescence after exposure to any of 266, 532 or 910 nm light. Hence, scattering and signal trapping were deduced to be the primary sources of interference. Measurements of the intensity in each channel were conducted with and without the presence of particles and/or toluene, to quantify the effect of these sources of interference on the collected signal. The results of these measurements are presented in Sect. 3.1.

2.4 Image processing and analysis

Each experimental run comprised of a series of raw images collected simultaneously from the two fluorescence emission channels, S_{315} and S_{285}, and from the scattering channel, S_{532}, which were processed to determine the temperature and particle number density using in-house MATLAB codes. A background image was measured for each channel from the time-average of 100 images collected under experimental conditions, except with the flow off and after all of the

Fig. 5 Spectral transmission efficiency of filter combinations used to form the two channels, S_{285} and S_{315}, for two-colour LIF thermometry. The combined filter transmission for each channel is calculated from data provided by the manufacturers (Asahi Spectra USA Inc. 2018; Semrock 2018)

Table 1 Optical filters used to form the two fluorescence channels, S_{285} and S_{315}, and one scattering channel, S_{532}. Abbreviations: *LP* long-pass filter, *SP* short-pass filter, *BP* band-pass filter, *BS* beam-splitter

S_{285}	S_{315}	S_{532}
2×275 nm LP	2×275 nm LP	2×275 nm LP
310 nm BS (reflected)	310 nm BS (transmitted)	310 nm BS (transmitted)
272 nm LP	355 nm BS (reflected)	355 nm BS (transmitted)
280 nm BP (20 nm width)	300 nm LP	532 nm BP
	300 nm BP (80 nm width)	
	330 nm SP	

toluene and particles had been flushed from the imaging region. This background image was subtracted from the raw images. Spatial matching of the cameras was done on a pixel-by-pixel basis utilising a two-stage approach. In the first stage, a target image was taken of a thin metal plate with an evenly spaced grid of small (2 mm) holes and notches. This was aligned such that the face was co-planar with the laser sheet. A UV lamp (Spectroline EB-160C) illuminated the plate from behind, with the transmitted light being imaged in S_{285} and S_{315} with the filters in place (the use of the filtered spectral bands for the target imaging was chosen to be identical to the actual experiment to prevent errors from chromatic aberrations). For S_{532} the same target was imaged using ambient lighting of the room. The channels S_{285} and S_{532} were spatially aligned to S_{315} by matching a series of corresponding points on each of the target images. The target images were recorded once per day with the same transformation matrices used for all images recorded on the same day. It is estimated that the resultant images after this stage were matched to within ± 1 pixel. A second stage image processing algorithm was utilised to further improve the spatial matching to sub-pixel accuracy. This was achieved for each image series using the time-averaged images of the toluene-seeded jet in which the averaged image from S_{285} was offset systematically in both the x and y directions in increments of 0.1 pixels using bi-linear interpolation. At each increment, the intensity ratio was calculated on a per-pixel basis using the offset image, and the standard deviation of an ensemble of pixels within the region $0.5 < x/D < 0.9$, $|r/D| < 1$ was calculated. This region was chosen because it is upstream of the heating laser (so the flow temperature is uniform) and includes the shear layer near to the jet exit plane where there were strong toluene concentration gradients (such that any alignment error significantly changes the ratio). The offset that resulted in the lowest standard deviation was selected to be used for all instantaneous images. This method was completed for each case with a resulting variance between all cases recorded in any single day of < 0.3 pixels. Over the course of a day, there was no clear trend in the changes to the value of the calculated offset, which suggests the variance is likely due to random error. For this reason, the mean of the offset calculated from all cases on one day was used to correct all images taken on that particular day.

The ratio S_{315}/S_{285} of each instantaneous image was then calculated for each spatially matched pixel. Data from S_{285} and S_{315} with an intensity below a threshold value of $15 \times$ the dark charge were removed from further analysis. This value was chosen for the threshold because previous work found that images for two-colour LIF with a signal to noise ratio of 15 were accurate to within 20 °C at a range of temperatures (Lewis et al. 2020). The resultant two-colour ratio image of S_{315}/S_{285} was corrected for systematic errors in the intensity ratio, such as can arise from spatial inhomogeneity in

camera response or spatial dependencies in the collection optics, using images taken under experimental conditions without particles or heating. This correction is based on the assumption that, without heating, the temperature in the measurement region is uniform at the ambient value. As such, the ratio calculated is expected to also be uniform, and any non-uniformity in the ratio is due to these systematic errors. This is similar to the correction performed by Jainski et al. (2014). The temperature was calculated from S_{315}/S_{285} using a linear curve fit of the calibration data (as presented in the Calibration section). The single-shot temperature images were smoothed using a 5×5 pixel median filter to reduce influence of noise on results, with a resultant decrease spatial resolution. The filter kernel size (5×5 pixels) was chosen to be close to the laser sheet thickness, giving an approximately cubic measurement volume. The median filter was selected (rather than other filters such as a mean filter) because it is less sensitive to the large fluctuations of values that may occur in the intensity ratio when the denominator term is small. The ambient temperature for each image set was calculated from the time-averaged temperature measured upstream of the heating laser.

The images of the Mie scattered signal (S_{532}) were used to determine the particle locations. After background correction and spatial matching, the images were corrected for variations of the laser sheet profile. The profile was estimated using the particle scattering intensity measured by the camera, averaged along the beam path. The images were then binarised using a threshold of $10 \times$ the standard deviation of the dark charge to ensure the signal from the particles was well separated from noise. The particle locations were then calculated from the intensity-weighted centroid of each particle in the binary mask. The instantaneous local particle number density was calculated by dividing each instantaneous image into an array of 21×21 pixel bins (corresponding to roughly $0.1D$), and then counting the number of particles within each bin.

2.5 Calibration

Calibration data was obtained by measuring the relationship between the gas temperature and the two-colour ratio S_{315}/S_{285} in the experimental system described above, except without the SSSTS beam or particles. Instead, the gas temperature was systematically varied over the range of 20 °C $< T_g <$ 160 °C using an electric tape heater (Briskheat BWH052100LD) fitted to the outside of the central pipe. Thermocouples mounted to the central pipe and in the centre of the jet flow at $x/D < 0.5$ were used to measure the outlet temperature of the gas and ensure the system had reached a steady state before the LIF measurements were recorded. The thermocouple in the jet was removed prior to measurements to prevent interference and flow disturbances, and

replaced after the measurement was completed to ensure there was no change in the flow temperature during the measurement. The time- and spatially averaged two-colour ratio measured at each flow temperature in the region of $0.6 < x/D < 1$, $|r/D| < 0.2$, where the temperature of the flow was spatially uniform, was used to calibrate the two-colour ratio to the thermocouple measured temperature.

The resultant calibration curve relating gas temperature to S_{315}/S_{285} is presented in Fig. 6, for gas temperatures in the range $20\ °C < T_g < 160\ °C$. The relationship between the intensity ratio of the two colours and the gas temperature is well described by a linear function of the form $S_{315}/S_{285} = 4.50 \times 10^{-3}\ T_g + 0.98$ ($R^2 = 0.9989$), for T_g in °C. We emphasise here that the constants in this relationship is valid only for the particular optical system employed here, because the ratio depends on the combination of cameras, filters and collection optics. However, the form of the relationship is expected to be general. The signal intensity measured in the channel S_{315} can be seen to decrease from 4.89×10^4 to 1.02×10^4 counts for $T_g = 21$ and $160\ °C$, respectively, while the intensity of S_{285} decreases from 4.54×10^4 to 6.07×10^3 over the same range. This decrease in intensity is due to the decrease in fluorescence quantum yield of toluene with temperature (Koban et al. 2004), which leads to an increase in the uncertainty of the measurements with temperature. Nevertheless, for all temperatures recorded here, the fluorescence emission intensity measured in both channels remains significantly (> 65 times) larger than the background. Although the flow temperature in the measurement region is uniform, there is a small variation in the spatially averaged measurement of S_{315}/S_{285} as a result of camera shot noise, background scatter, electronic noise and
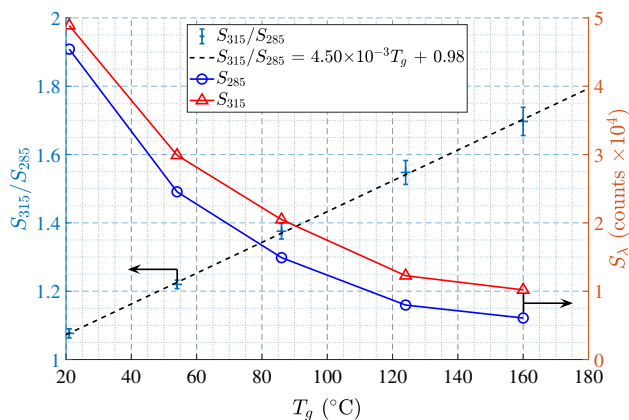

Fig. 6 The relationship between gas temperature and S_{315}/S_{285} (+), together with a linear fit of the measured data (black dashed line). The error bars correspond to the image-to-image standard deviation in the measured ratio at each temperature. The dependence on temperature of the fluorescence intensity of S_{315} ($\triangle$) and S_{285} ($\bigcirc$) is also presented. For reference, the time- and spatially averaged dark charge signals measured in S_{285} and S_{315} were 90 and 92 counts, respectively

sub-pixel misalignment of the two fluorescence images. The combined influence of these uncertainties leads to an image-to-image standard deviation of S_{315}/S_{285} of 1.2% at 21 °C increasing to 2.4% at 160 °C, with the latter due to the strong decrease in fluorescence signal with temperature. This variation corresponds to an uncertainty of the spatially averaged measured temperature of 3 °C and 9 °C at flow temperatures of 21 °C and 160 °C, respectively.

3 Results

3.1 Uncertainty analysis

3.1.1 Systematic errors

The accuracy of the current two-colour LIF measurements was estimated using images of the mean and instantaneous images of the unheated flow (i.e. a flow at uniform ambient temperature). Table 2 presents the results of a systematic study of the intensity recorded with each camera for a range of cases with and without the presence of toluene, particles and laser beams in the measurement region. These measurements consist of the time- and spatially averaged intensity count, S_λ, in a 195×117 pixel region intersected by all lasers, i.e. the region $|r/D| < 0.3$ and $1 < x/D < 2$ (see also Fig. 2), for the cases with and without the various lasers switched on. Cases 1–3 (rows 1–3) are for the flow without toluene with the conditions chosen to identify if scattering from particles or stray light is detected in any of the channels. Cases 4 and 5 have toluene seeded in the flow with the conditions chosen to identify whether or not the presence of the 532 and 910 nm lasers, with or without particles, affect the fluorescence signals, and also whether or not the fluorescence emissions generate significant interference to the S_{532} measurement. Case 1 presents the dark charge signal, here denoted as $S_{\lambda,DC}$. The signals measured with each camera for Cases 2 to 5 are normalised by $S_{\lambda,DC}$. The signal measured with S_{532} for the cases where the flow contains particles and with the 532 nm beam on (Cases 3 and 5) are not presented because the measurement is the spatial average of the scattering signal from disperse particles, which does not provide an accurate indication of the signal from individual particles. The results for each case are summarised below.

- The dark charge signals for each camera, presented in case 1 (row 1 in Table 2), were $S_{285,DC} = 90.1$ counts, $S_{315,DC} = 92.2$ counts and $S_{532,DC} = 398.9$ counts. Both S_{285} and S_{315} were recorded using 16-bit cameras, while S_{532} was recorded using a 14-bit camera.
- Case 2 presents the background noise, which is the measured signal with the lens uncapped and the diagnostic laser beams on with pulse energies identical to

Table 2 The conditions under which a series of experiments were performed to assess interference, measured by each camera in the imaged region aligned with the all lasers (S_λ). For the dark charge (row 1) the average intensity in counts (cts) is presented. The intensity is normalised by that of the dark charge for each other case. The 910 nm laser is the heating beam from the SSSTS. The data for S_{532} for the cases with both particles and the 532 nm laser are not presented (N.P.) because this method does not give a useful indication of the signal from individual particles

Case	Toluene	Particles	Laser (nm)			$S_{285,DC}$ (cts)	$S_{315,DC}$ (cts)	$S_{532,DC}$ (cts)
			266	532	910			
1	☐No	☐No	☐No	☐No	☐No	90.1	92.2	398.9
						$S_{285}/S_{285,DC}$	$S_{315}/S_{315,DC}$	$S_{532}/S_{532,DC}$
2	☐No	☐No	☐Yes	☐Yes	☐No	1.01	1.05	1.00
3	☐No	☐Yes	☐Yes	☐Yes	☐Yes	1.00	1.00	N.P
4	☐Yes	☐No	☐Yes	☐No	☐No	349	378	1.00
5	☐Yes	☐Yes	☐Yes	☐Yes	☐No	326	361	N.P

the main experiments but with no flow. It can be seen that this results in a 5% increase in S_{315} relative to the dark charge, but no significant increase for the other channels. This small increase in S_{315} is insignificant compared to the toluene signal (rows 4 and 5), which shows that ambient light and background laser light were effectively suppressed.

- For case 3 the diagnostic lasers and SSSTS beam were switched on with the particles seeded into the flow. It can be seen that no measurable increase is recorded for S_{285} or S_{315}, which shows that the elastic scattering of all laser wavelengths from particles was effectively suppressed by the optical filters used to form the LIF channels.

- For case 4 toluene was seeded in the flow with only the 266 nm laser switched on. It can be seen that the fluorescence emissions of toluene in this region were 349 and 378 times stronger than the dark charge for S_{285} and S_{315}, respectively. There was no increase in the signal for S_{532}, which demonstrates that the fluorescence emissions were effectively suppressed in this channel.

- Case 5 presents the signal from the flow with both toluene and particles seeded while the 266 nm and 532 nm lasers were switched on. The reduction in both S_{285} and S_{315} compared to case 4 is similar so that the resultant ratio $S_{315}/S_{285} = 1.133$ for case 5, which is only 2.2% greater than for case 4, with $S_{315}/S_{285} = 1.108$. This increase is a systematic error due to the interference of particles, through the combined effects of signal trapping, attenuation and multiple scattering. The resultant error in the temperature measurement is $+5.5\,°C$ at 28 °C and, assuming that this error is not strongly influenced by temperature, a $+8\,°C$ error at 150 °C.

3.1.2 Random errors

The random error in the intensity ratio S_{315}/S_{285} was estimated using the standard deviation of S_{315}/S_{285} (σ_R) in the ensemble of pixels within the region near to the jet exit of $0.5 < x/D < 0.7$ and $|r/D| < 0.1$. This region was chosen because the toluene concentration here is the highest in the flow and close to uniform, with the time-averaged fluorescence signal here > 25,000 counts for both S_{315} and S_{285}. For the unheated flow without particles (case 4 of Table 2) the standard deviation of the intensity ratio in this region was $\sigma_R = 0.088$, which corresponds to a standard deviation in the derived temperature of $\sigma_T = 21\,°C$ for a flow temperature of $T_g = 25\,°C$. The standard deviation of the fluorescence signals measured in this region for S_{285} and S_{315} were $\sigma_{285} = 1,790$ counts and $\sigma_{315} = 1,970$ counts, respectively. While these variations in the fluorescence signal are expected to decrease with the signal S_λ i.e. in regions with lower toluene concentration or at higher temperature, here we conservatively assume that σ_{285} and σ_{315} are constant for all fluorescence intensities. The lowest fluorescence signal measured for any heating flux in the region of $0.5 < x/D < 3.7$ and $|r/D| < 0.5$ is $S_{285} \approx 10,000$ counts, therefore the maximum relative standard deviations for the fluorescence channels are estimated to be $\frac{\sigma_{285}}{S_{285}} \approx 0.179$ and $\frac{\sigma_{315}}{S_{315}} \approx 0.197$. If the random noise is modelled a Gaussian distribution with standard deviation σ_λ for each channel, the maximum standard deviation of the temperature measurement can be numerically calculated to be $\sigma_T \approx 48\,°C$ for $T_g = 25\,°C$ and $\sigma_T \approx 94\,°C$ for $T_g = 150\,°C$.

For the unheated flow with particles (case 5 of Table 2), the results show that the standard deviation of the measured intensity ratio in the region of $0.5 < x/D < 0.7$ and $|r/D| < 0.1$ increases slightly to $\sigma_R = 0.110$ ($\sigma_T = 24\,°C$). The estimated maximum uncertainty, for the particle-laden flow with $S_{285} \approx 10,000$ counts, is $\sigma_T = 60\,°C$ for $T_g = 25\,°C$ and $\sigma_T =$

118 °C for T_g = 150 °C. While the uncertainties in the instantaneous pixel-to-pixel temperatures are relatively high, they are reduced significantly through time averaging. In the present experiments the time averaged data uses greater than 100 images for each case, and hence the uncertainty in the temperature reduces to $\frac{\sigma_{\overline{T}}}{\sqrt{100}}$ = 11.8 °C.

3.2 Instantaneous temperature measurements

Figure 7 presents typical single-shot images of S_{285} and S_{315}, together with the temperature image and the binary particle mask from S_{532}, for three flow cases. One case without particles but with radiant heating (top row) and two cases with particles, one without (middle row) and the other with radiant heating (bottom row). The heating flux was $\dot{Q}''_{peak}$ = 42.8 MW/m² for the cases with radiant heating
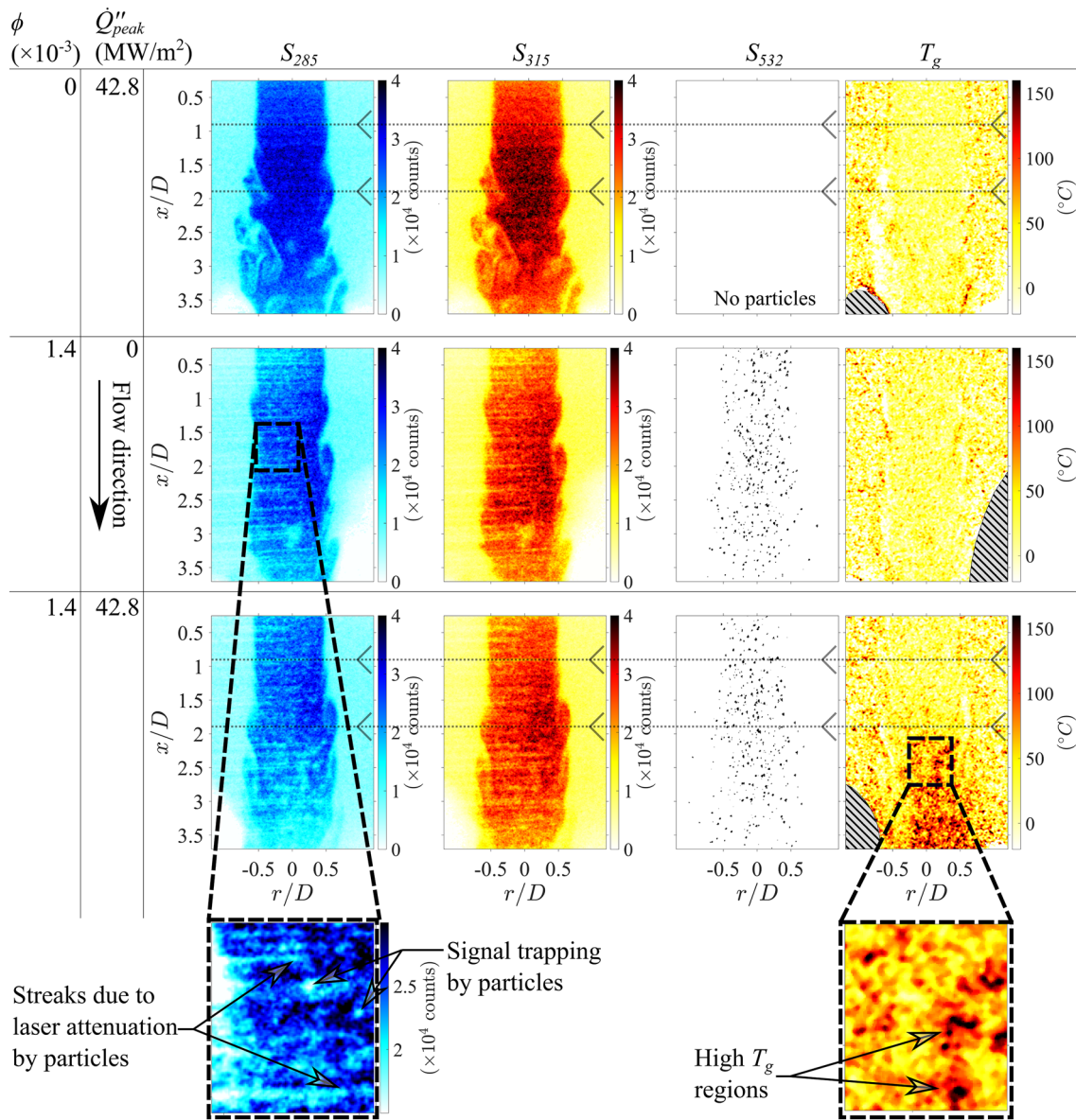

Fig. 7 Typical single-shot images from each camera and the resultant temperature calculated from S_{315}/S_{285}. The top row has an instantaneous particle loading of $\phi = 0$ and a heating flux of $\dot{Q}''_{peak}$ = 42.8 MW/m². The middle and bottom rows have an instantaneous loading of ϕ = 1.4×10⁻³ with $\dot{Q}''_{peak}$ = 0 and 42.8 MW/m², respectively. The dotted lines indicate the location and direction of the SSSTS beam. The zoomed insets show interesting features of laser attenuation and sig-nal trapping due to particles in the fluorescence channels (left, noting the colour scale is different to the main figure to improve the clarity of the features), as well as highly localised regions of high temperature that are present for $\dot{Q}''_{peak}$ = 42.8 MW/m² (right). The cross-hatched areas correspond to regions where the signal from one or both of S_{285} and S_{315} are below the minimum threshold for reliable measurements

while for the latter two cases the instantaneous particle volumetric loading was $\phi = 1.4 \times 10^{-3}$, which is sufficiently high for the particle-laden flow to be in the four-way coupling regime (Elgobashi 2006). In this and subsequent figures the location and direction of the incident SSSTS beam are indicated by the dotted lines and arrowheads, with the SSSTS beam direction from the right to the left of the image (positive to negative r/D).

The fluorescence signal measured with the channels S_{285} and S_{315} is highly variable over the imaging region, due to the combined influences of variations in toluene concentration, laser fluence and temperature. The initial toluene concentration differs for the jet (0.75%) and the co-flow (0.25%), with inhomogeneity further increased downstream due to mixing in the shear layer and jet spreading. The local fluence of the 266 nm laser varies by approximately 25% in the axial direction due to the non-uniform laser sheet intensity profile. The fluence also decreases by approximately 20% across the jet along the excitation beam path length due to attenuation by the particles and absorption by the toluene. However, the spatial variations in the fluorescence signal due to the variations in toluene concentration and laser fluence are equal in both channels and are cancelled out in the two-colour ratio used to derive the temperature. This demonstrates the advantages of using the two-colour ratio method over seeking to deduce the temperature from a single wavelength. The emission intensity also decreases with increasing temperature, which can be seen in the images of S_{285} and S_{315} downstream from the heating region ($x/D > 0.9$). The intensity in this region is much lower for $\dot{Q}''_{peak} = 42.8$ MW/m^2 than for $\dot{Q}''_{peak} = 0$ MW/m^2 despite exhibiting a similar signal strength for $x/D < 0.9$.

The effect of attenuation of the excitation laser sheet by particles can be seen by comparing the fluorescence emission images in the top row of Fig. 7, for which there are no particles in the flow, with the other two rows. The attenuation by the particles in the laser sheet can be seen to be significant from the horizontal streaks of low intensity (shadows), which occur down-beam from particles. The particles have a mean diameter of 173 μm, which is about one quarter of the thickness of the laser sheet (approximately 600 μm).This implies that the shadow down-beam from a single particle within the beam typically attenuates up to 25% of the laser excitation. However, even greater attenuation may be generated by the largest particles ($d_p \sim 300$ μm), agglomerated particles or by clusters of particles in close proximity. Circular regions of lower signal can also be seen, without a corresponding streak. These regions can be attributed to signal trapping by particles between the laser sheet and the collection optics, some of which result in strong attenuation of the fluorescence signal. These issues highlight the importance of the present optical arrangement in which the use of the beam-splitter to separate the two channels means that both cameras collect signals from an identical optical path through the flow. In this way, effects such as signal trapping are the same in both channels and the temperature can still be measured. Nevertheless, the measurement uncertainty in these regions with attenuation is increased because of the reduction in the signal to noise ratio. Locations of both attenuation and signal trapping by the particles are identified in the bottom-left zoomed image of S_{285} in Fig. 7.

For the case with particles in the flow and the heating laser operating at a flux of $\dot{Q}''_{peak} = 42.8$ MW/m^2, T_g can be seen to increase significantly with axial distance for $x/D > 1.5$. Most of the temperature rise can be seen to occur downstream from the region $0.9 < x/D < 1.9$ where the radiative heating is applied. No temperature gradients can be seen for the case with the heating laser on but without particles. This result is consistent with expectation, given that there is no significant absorption of the heating beam by the toluene or nitrogen. Instantaneous local temperatures of up to 150 °C are prevalent in the heated case, with these regions of high temperature corresponding to locations with high local particle number density. Importantly, significant inhomogeneity in the temperature immediately downstream from the heating region can be seen in the zoomed image with regions of T_g spanning the entire range from ambient to 150 °C. This demonstrates that the time scale for the particles to transfer heat to the gas phase by convection is significantly longer than that required to heat the particles by radiation, as expected. Significant inhomogeneity in the gas-phase temperature persists even to the downstream edge of the image, $x/D = 3.5$, although it is somewhat reduced due to the influence of gas-phase mixing. These localised regions of high temperature remaining coherent downstream of the heating region indicates that the gas-phase heat transfer and/or mixing across the large flow length scales in the jet is relatively minor.

Random errors in the measurement can be seen in the temperature image for the case without heating, for which the flow is at uniform temperature. These measurement errors are most significant outside of the central jet flow ($|r/D| > 0.5$) because of the low fluorescence signal in the weakly seeded annular flow. The measured temperature is of less interest in this region than for the central jet flow because there are few, if any, particles present. In the central jet flow for the case without heating but with particles, the standard deviation of the measured temperature in the ensemble of pixels bounded by the region of $0.5 < x/D < 3.7$ and $|r/D| < 0.5$ was $\sigma_T = 17.8$ °C.

3.3 Time averaged results

Figure 8 presents the time-averaged images of gas-phase temperature above ambient $\overline{T}_g - T_a$, where the overbar denotes time-averaged values, for a series of cases with the particle-laden jet heated by the SSSTS at fluxes of $\dot{Q}''_{peak} = 0$, 13.7, 29.4, 36.3 and 42.8 MW/m². The time-averaged particle volumetric loading for each case presented was $\phi = 1.4 \times 10^{-3}$. It can be seen that the gas temperature is uniform across the jet in the region upstream of the SSSTS beam, i.e. for $x/D < 0.9$, in all cases. The temperature rise within the zone of irradiation is small, but becomes significant and continues to increase both with axial distance and heating flux. This lag can be attributed to the combination of two time constants, firstly, of the particles to reach their peak temperature whilst being heated by the SSSTS and, secondly, the convective heat transfer between the particles and gas. The gas temperature can be seen to increase with axial distance to the edge of the measurement region, which indicates that the particles are significantly hotter than the gas all the way to $x/D = 3.7$. Indeed, this also suggests that the gas temperature continues to rise beyond the measurement region investigated here.

The gas temperature is found to be non-uniform in the radial direction, with a maximum near to the centreline and with a higher average temperature measured for $r/D > 0$ than for $r/D < 0$. The gradients away from the axis can be attributed to shear-driven mixing with the ambient co-flow surrounding the jet, which is consistent with well-known trends in scalar mixing in jets (Mi et al. 2001). However, radial gradients in particle concentration may also play a role (Lau and Nathan 2016). The trend of lower temperatures on the down-beam side of the SSSTS can be attributed to shadowing effects, where the particles nearer the radiation source are subject to a higher flux than those behind. The greatest value of $\overline{T}_g - T_a$ was 86.1 °C, which occurs for the peak flux

of $\dot{Q}''_{peak} = 42.8$ MW/m², at the location $x/D = 3.69$, $r/D = 0.11$. The off-axis location of the peak temperature (i.e. $r/D = 0.11$) found here is consistent with the influence of particle attenuation that can be seen in Fig. 7. The temperatures for the other heating fluxes at $x/D = 3.69$ and $r/D = 0.11$ were measured to be $\overline{T}_g - T_a = 62.1$, 50.8 and 25.8 °C for $\dot{Q}''_{peak} = 36.3$, 29.4 and 13.7 MW/m², respectively.

Figure 9 presents the change in power from the SSSTS due to attenuation by the particles $\Delta\dot{Q} = \dot{Q}_0 - \dot{Q}_p$, where $\dot{Q}_0$ and $\dot{Q}_p$ are the time-averaged powers recorded using the power meter down-beam of the wind tunnel for $\phi = 0$ and 1.4×10^{-3}, respectively. It can be seen that $\Delta\dot{Q}$ increases linearly with $\dot{Q}_0$, as expected. The presented values of $\dot{Q}_0 = 910$, 1950, 2410 and 2840 W correspond to peak heating fluxes of $\dot{Q}''_{peak} = 13.7$, 29.4, 36.3 and 42.8 MW/m², respectively. The fraction of the beam power attenuated by the particles, $\Delta\dot{Q}/\dot{Q}_0$, is presented in the inset of Fig. 9. It can be seen that $\Delta\dot{Q}/\dot{Q}_0$ increases from 0.17 to 0.21 as $\dot{Q}_0$ is
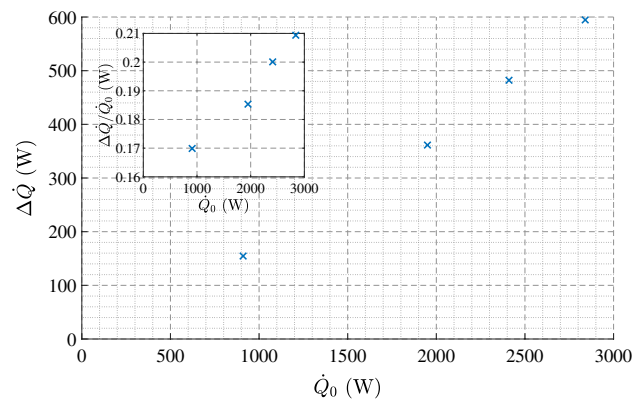
Fig. 9 Attenuated power of the heating beam by the particle-laden flow for $\phi = 1.4 \times 10^{-3}$ ($\Delta\dot{Q}$), as a function of the power for $\phi = 0$ ($\dot{Q}_0$). Inset is the fraction of the heating beam that is attenuated, $\Delta\dot{Q}/\dot{Q}_0$
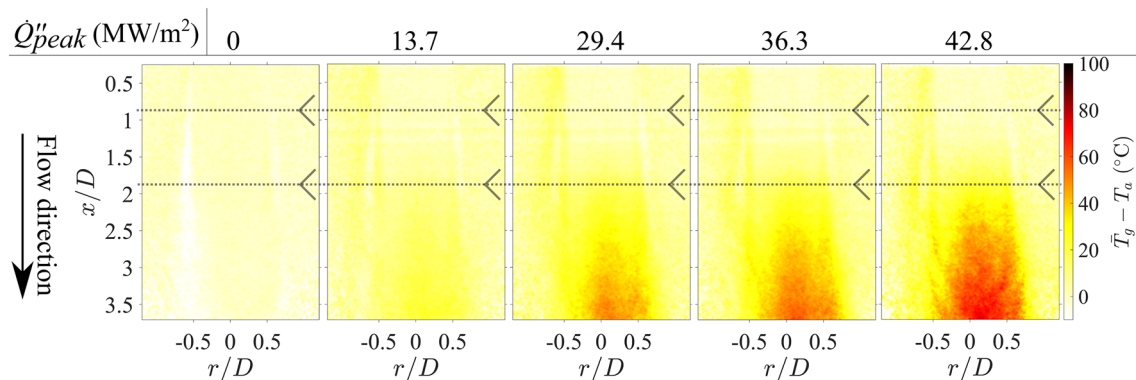
Fig. 8 Time-averaged images of gas temperature above ambient, $\overline{T}_g - T_a$ for a mean particle loading of $\overline{\phi} = 1.4 \times 10^3$ at a series of heating fluxes, $\dot{Q}''_{peak}$. The dotted lines indicate the location and direction of the SSSTS beam

increased from 910 to 2840 W. A possible reason for this is the influence of temperature on the absorption cross section of the particles, which has been previously demonstrated by Zhao et al. (2020) albeit with different particle materials.

The predicted attenuation of a beam through a particle-laden flow can be estimated using the Beer–Lambert law, given by $\Delta\dot{Q}/\dot{Q}_0 = 1 - \exp\left(-A_{p,1}l\overline{\phi}/V_{p,1}\right)$, where $A_{p,1}$ and $V_{p,1}$ are the projected area and volume of a single particle, respectively, and l is the path length of the beam through the flow (Kalt et al. 2007). For a path length corresponding to the inner diameter of the pipe, $l = D = 12.6$ mm, a particle volumetric loading of $\phi = 1.4 \times 10^{-3}$ and assuming the particles are spherical with a diameter distribution corresponding to that presented in Fig. 3, the attenuation is estimated to be $\Delta\dot{Q}/\dot{Q}_0 = 0.156$. This is slightly lower than the measured $\Delta\dot{Q}/\dot{Q}_0$, although this simplified prediction does not take into account the non-uniform heating laser profile. Despite these assumptions, the calculated value is sufficiently close to the measurement to provide further confidence in the measured values of $\Delta\dot{Q}/\dot{Q}_0$.

The time-averaged particle number density (N), normalised by the number density on the centreline (N_c), at $x/D = 0.5$ with $\dot{Q}''_{peak} = 0$ is presented in Fig. 10 (top). Also included in the figure are the particle concentration profiles measured near to the jet exit plane by Tsuji et al. (1988) for $Sk_D \approx 800$ and $Re_D \approx 26{,}000$, together with those by Lau and Nathan (2016) for $Sk_D = 22$ and $Re_D = 40{,}000$. Hence these are somewhat different from the current flow, with $Sk_D = 77$ and $Re_D = 3{,}000$. It can be seen that the results are broadly consistent, with a weak peak on the axis and a slight decay toward the edges of the jet, despite some differences that can be attributed to the different Stokes and Reynolds numbers already noted. For example, both Sk_D and Re_D have been shown to significantly influence particle number density at the jet exit (Lau and Nathan 2016). Furthermore, the current data is expected to be noisier than the previous data, particularly those by Lau and Nathan (2016), because relatively fewer particles are measured in the current measurements owing to the larger particle diameters. In any case, the present results show that at $x/D = 0.5$ the value of N/N_c is greatest on the jet centreline and exhibits only a slight decrease with radial distance to $r/D = 0.3$, with N/N_c decreasing to $N/N_c \approx 0.8$ in this region. Beyond this for $r/D > 0.3$, N/N_c sharply drops towards zero at $r/D \approx 0.6$, as expected.

Figure 10 also presents the normalised number density measured at $x/D = 1.5$ (middle) and $x/D = 3$ (bottom), for both $r/D > 0$ and $r/D < 0$, with $\dot{Q}''_{peak} = 0$ and 42.8 MW/m^2. The broad trends observed at $x/D = 0.5$ are also observed at $x/D = 1.5$ (which is near to the centre of the heating region) although the jet has spread slightly such that N/N_c approaches zero at $r/D \approx 0.8$. The particles being predominantly concentrated near to the jet axis is consistent with
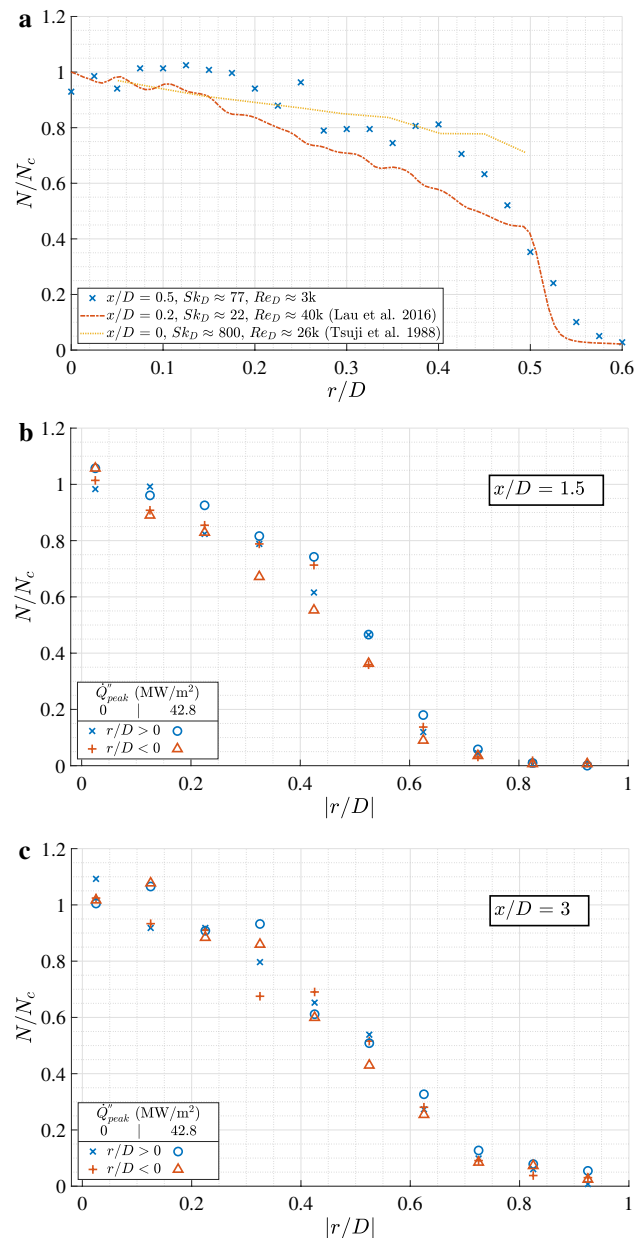

Fig. 10 Radial particle number density, N, normalised by the centreline value, N_c, measured from particle scattering images recorded simultaneously with the fluorescence images. The top sub-figure presents the radial profile near to the jet exit for the current experiments along with the particle concentration measured by Tsuji et al. (1988) and Lau and Nathan (2016) in a particle-laden pipe jet. The bottom two sub-figures present the radial profiles measured at $x/D = 1.5$ (middle) and $x/D = 3$ (bottom), $r/D < 0$ and $r/D > 0$, for a mean particle loading of $\phi = 1.4 \times 10^3$, and for $\dot{Q}''_{peak} = 0$ and 42.8 MW/m^2

the temperature measurements (Fig. 8), which also shows that the gas temperature approaches a local maximum near to the jet axis. The radial profiles of N/N_c are similar for both $r/D < 0$ and $r/D > 0$, demonstrating that the particle number density is symmetrical about the jet axis despite the radial asymmetry that can be seen in the temperature

images (Fig. 8). This shows that the radial bias for the temperature measurements is not due to a similar bias in the particle concentrations. The results also show that the radial particle number density profile is broader at $x/D = 3$ than for $x/D = 1.5$, and that the profile transitions toward shallower gradients consistent with well-known jet spreading trends in single- and two-phase jets. Importantly, the radial number density profiles do not change significantly with heating flux within the axial range investigated here, which implies that neither heating-induced buoyancy nor heating-induced turbulence have any significant influence on lateral migration for these particles within this region.

The profiles of the measured temperature above ambient, $\overline{T}_g - T_a$, on the jet centreline for $0 \leq \dot{Q}''_{peak} < 42.8$ MW/m^2, with a fixed particle loading of $\phi = 1.4 \times 10^{-3}$, are presented in Fig. 11. Also presented is the temperature change normalised by the heating flux, $\left(\overline{T}_g - T_a\right)/\dot{Q}''_{peak}$. The shaded area of the figure indicates the location and intensity of the heating beam. The results show that the gas temperature remains close to the ambient $\left(\overline{T}_g - T_a \approx 0\right)$ both upstream from and within the beginning of the region with the heating laser, i.e. for $x/D < 1.1$, for all heat fluxes. Downstream from this, $\overline{T}_g$ increases monotonically within the measurement region for all $\dot{Q}''_{peak} > 0$ MW/m^2, due to the heat transfer from the heated particles to the gas. It should also be noted that the high-flux radiation from the SSSTS is in the region $0.9 < x/D < 1.9$, with the peak flux at $1.24 < x/D < 1.56$ (see also the profile presented in Fig. 4). Thus there is a slight lag of approximately $0.2D$ between the initial radiation absorption and an observable increase of $\overline{T}_g$. Importantly, the normalised data, presented in the inset, show excellent collapse giving strong confidence in the measured results.

Figure 11 also shows that the rate of temperature rise increases with $\dot{Q}''_{peak}$, as expected, and that the temperature continues to increase near-linearly with axial distance downstream of the heating beam to the edge of the measurement region ($1.9 < x/D < 3.7$). This suggests that the gas temperature will continue to increase for some distance downstream since the temperature gradient will approach zero when its temperature equilibrates that of the particles. These measurements are also consistent with the expectation that the particles have a higher temperature than the average gas temperature throughout the region for all heating fluxes, owing to the radiation being absorbed by the particles and transferred to the gas.

Near to the downstream end of the measurement region, at $x/D = 3.5$ (which is 32.8 mm from the upstream edge of the heating region), $\overline{T}_g - T_a = 67.7$ °C for $\dot{Q}''_{peak} = 42.8$ MW/m^2. At this axial location, $\overline{T}_g - T_a = 57.0, 48.7$ and 22.4 °C for $\dot{Q}''_{peak} = 36.3, 29.4$ and 13.7 MW/m^2, respectively. The normalised temperature curves presented in the inset of Fig. 11 confirm the linear relationship between gas temperature rise and the heat gain of the particle phase by radiation absorption (i.e. $\Delta T_g \propto T_p - T_g$, where T_p is the particle temperature), since $T_p - T_a \propto \dot{Q}''_{peak}$. This is consistent with convection being the dominant mode of heat transfer between the heated particles and the gas and also implies that radiant cooling of the particles is negligible. That is, particle temperatures are not sufficiently high for radiation to be significant, consistent with the maximum value of $\overline{T}_g - T_a$ being 67.7 °C.

The rate of change of the centreline temperature with axial distance ($d\overline{T}_g/dx$), averaged over two separate regions of $1 < x/D < 2$ and $2 < x/D < 3$, are presented in Fig. 12 for all fluxes. The region centred at $x/D = 1.5$ is mostly comprised of the heating region, while the region centred at $x/D = 2.5$ has no radiative heat input. The rate $d\overline{T}_g/dx$ increases
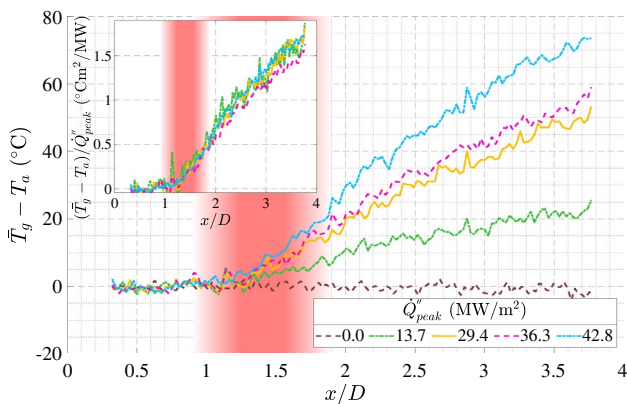
Fig. 11 The measured gas temperature above ambient against axial distance on the jet centreline for a series of heating fluxes, with a mean volumetric loading of $\phi = 1.4 \times 10^{-3}$ along with the centreline temperature normalised by the heating flux in the inset figure. The shaded areas indicate the SSSTS beam location and intensity
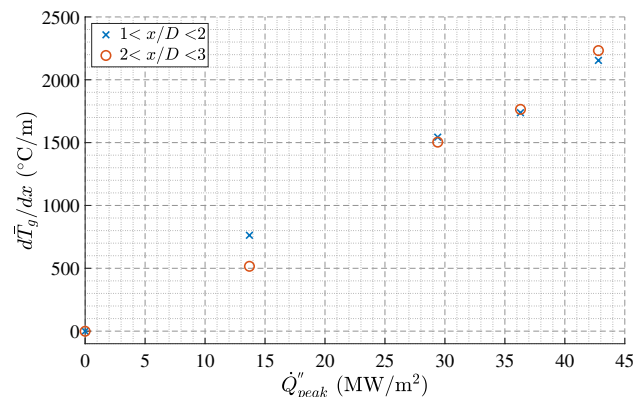
Fig. 12 The measured axial temperature gradient as a function of radiation heat flux within two axial regions of the flow, $1 < x/D < 2$ and $2 < x/D < 3$

monotonically with $\dot{Q}''_{peak}$ and is similar for both axial locations. The greatest measured rate of temperature increase was $d\overline{T}_g/dx = 2{,}200$ °C/m for $\dot{Q}''_{peak} = 42.8$ MW/m^2. Assuming a constant gas velocity in this region of 3.6 m/s (from the bulk velocity), the corresponding rate of gas temperature increase at this flux is approximately 8,000 °C/s. This is comparable to the particle temperature gain, for a different particle material and diameter, measured under similar conditions of 23,000 °C/s (Kueh et al. 2017).

The radial profiles of mean (time-averaged) temperature above ambient, $\overline{T}_g - T_a$, at a series of axial distances for $\dot{Q}''_{peak} = 42.8$ MW/m^2 (top) and for a series of heating fluxes at $x/D = 3$ (bottom) are presented in Fig. 13. The inset of the bottom sub-figure presents the temperature above ambient normalised by the heating flux. From both sub-figures it can be seen that the radial bias in temperature is consistent with the direction of the incident SSSTS beam, which is from positive r/D to negative (right to left in the figure). This confirms the significant role of attenuation of the SSSTS beam at the particle loading used in the current experiment
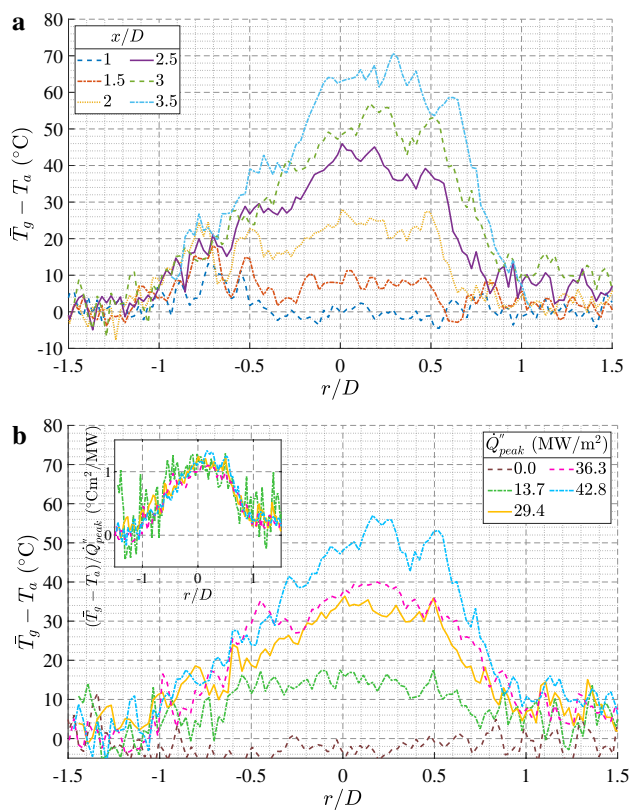
Fig. 13 Measured time-averaged radial profiles of gas temperature above ambient for a range of axial distances with $\dot{Q}''_{peak} = 42.8$ MW/ m^2 (top) and for all heat fluxes analysed at $x/D = 3$ (bottom). The inset of the bottom sub-figure presents the temperature above ambient normalised by the heating flux for the same conditions in the bottom sub-figure

($\overline{\phi} = 1.4 \times 10^{-3}$). The resultant temperature is significantly different for $r/D = 0.4$ and $r/D = -0.4$, with $T_g - T_a = 70.7$ °C and 38.0 °C, respectively, at $x/D = 3.5$ for $\dot{Q}''_{peak} = 42.8$ MW/m^2. The temperature for $r/D > 0$ continues to increase with x/D throughout the measurement region, while for $r/D < -0.3$ there is little change from $x/D = 3$ to $x/D = 3.5$. The radial temperature profiles normalised by heating flux also collapse well here, which is consistent with the centreline temperature profiles in Fig. 11.

4 Conclusion

A spatially resolved, planar measurement of the instantaneous gas-phase temperature, together with the particle number density, has been demonstrated using two-colour laser-induced fluorescence and Mie scattering within a particle-laden jet flow heated using high-flux radiation, for a series of heating fluxes up to $\dot{Q}''_{peak} = 42.8$ MW/m^2. The elastically scattered laser light from the particles, which were seeded at a sufficiently high loading for the flow to be in the four-way coupling regime, was shown to be effectively suppressed by the optical filters for each of the two-colour LIF channels. The signal-to-noise ratio of the fluorescence emissions for the flow without particles was measured to be ≥ 349 for both channels, giving confidence in the method. For the case with particles in the flow and radiative heating the fluorescence signal could be seen to decrease by $< 7\%$, which was attributed to a combination of the decrease in fluorescence quantum yield of toluene with temperature, the attenuation of the excitation laser and signal trapping by particles. For a typical instantaneous image the two-colour LIF method was found to have a pixel-to-pixel standard deviation, for an isothermal flow with the particles seeded at $\overline{\phi} = 1.4 \times 10$–3, of 17.8 °C, despite the significant fluctuations in the fluorescence signal due to mixing of the flow, laser attenuation and signal trapping. This demonstrates the advantage of the two-colour method for such applications in that the dependence of temperature on the ratio of two wavelengths results in the effects of attenuation being cancelled out, provided that the two wavelengths are collected from a common optical path.

For the present system, with particles of mean diameter 173 μm and a bulk flow velocity of 3.6 m/s, instantaneous gas temperatures of up to 125 °C above ambient were measured locally for a peak heating flux of $\dot{Q}''_{peak} = 42.8$ MW/m^2 irradiating a transverse region of approximately 11 mm in diameter. These peak temperatures were found to occur in highly localised regions where the local particle volumetric loading was also simultaneously high. The time-averaged temperature was found to increase linearly with both heating flux and distance downstream from the heating region, with

the gas temperature continuing to increase to the end of the measurement domain. A mean temperature increase of 67.7 °C above ambient was measured on the jet centreline at $x/D = 3.5$ (which is 32.8 mm downstream from the start of the heating region), also for $\dot{Q}''_{peak} = 42.8$ MW/m². This corresponds to an average heating rate of approximately 2,200 °C/m for the gas.

The derived temperature images were found to provide several new insights into the heat transfer processes that occur in particle-laden flows subjected to high-flux radiation. The localised regions of high temperature could be seen to remain coherent well downstream of the heating region, indicating that there is relatively little gas-phase heat transfer and mixing across length scales within the measurement region associated with large-scale turbulence. The temperature of the gas was also found to be higher on the side of the jet closest to the radiative heating source, which can be attributed to the heating beam being absorbed and/or scattered by the particles, consistent with expectation. It was also found that the particle number density was not significantly influenced by the presence of high flux radiative heating, within the measurement region investigated for heat fluxes up to $\dot{Q}''_{peak} = 42.8$ MW/m². This suggests that any effects of buoyancy-induced acceleration are small for the conditions investigated here.

Data availability Available upon request.

Declarations

Conflict of interest Authors declare that they have no conflict of interest.

References

Abram C, Fond B, Beyrau F (2017) Temperature measurement techniques for gas and liquid flows using thermographic phosphor tracer particles. Prog Energy Combust Sci 64:93–156. https://doi.org/10.1016/j.pecs.2017.09.001

Alwahabi ZT, Kueh KCY, Nathan GJ, Cannon S (2016) Novel solid-state solar thermal simulator supplying 30,000 suns by a fibre optical probe. Opt Express 24:A1444–A1453. https://doi.org/10.1364/OE.24.0A1444

Asahi Spectra USA Inc. (2018) UV Longpass Filters. https://www.asahi-spectra.com/opticalfilters/uv_longpass_filters.html

Banko AJ, Villafañe L, Kim JH, Eaton JK (2020) Temperature statistics in a radiatively heated particle-laden turbulent square duct flow. Int J Heat Fluid Flow 84:108618. https://doi.org/10.1016/j.ijheatfluidflow.2020.108618

Berrocal E, Kristensson E, Richter M, Linne M, Aldén M (2008) Application of structured illumination for multiple scattering suppression in planar laser imaging of dense sprays. Opt Express 16:17870–17881. https://doi.org/10.1364/OE.16.017870

Chen H, Chen Y, Hsieh H-T, Siegel N (2006) Computational fluid dynamics modeling of gas-particle flow within a solid-particle solar receiver. J Sol Energy Eng 129:160–170. https://doi.org/10.1115/1.2716418

Cundy M, Trunk P, Dreizler A, Sick V (2011) Gas-phase toluene LIF temperature imaging near surfaces at 10 kHz. Exp Fluids 51:1169–1176. https://doi.org/10.1007/s00348-011-1137-8

Davis D, Muller F, Saw W, Steinfeld A, Nathan G (2017) Solar-driven alumina calcination for CO2 mitigation and improved product quality. Green Chem 19:2992–3005. https://doi.org/10.1039/c7gc00585g

Eaton JK, Fessler JR (1994) Preferential concentration of particles by turbulence. Int J Multiph Flow 20:169–209. https://doi.org/10.1016/0301-9322(94)90072-8

Elgobashi S (2006) An Updated Classification Map of Particle-Laden Turbulent Flows. In: Balachandar S, Prosperetti A (eds) IUTAM Symposium on Computational Approaches to Multiphase Flow: Proceedings of an IUTAM Symposium held at Argonne National Laboratory, October 4–7, 2004. Springer Netherlands, Dordrecht, pp 3–10

Evans G, Houf W, Greif R, Crowe C (1987) Gas-particle flow within a high temperature solar cavity receiver including radiation heat transfer. J Sol Energy Eng 109:134–142. https://doi.org/10.1115/1.3268190

Faust S, Goschütz M, Kaiser SA, Dreier T, Schulz C (2014) A comparison of selected organic tracers for quantitative scalar imaging in the gas phase via laser-induced fluorescence. Appl Phys B 117:183–194. https://doi.org/10.1007/s00340-014-5818-x

Frankel A, Pouransari H, Coletti F, Mani A (2016) Settling of heated particles in homogeneous turbulence. J Fluid Mech 792:869–893. https://doi.org/10.1017/jfm.2016.102

Jainski C, Lu L, Sick V, Dreizler A (2014) Laser imaging investigation of transient heat transfer processes in turbulent nitrogen jets impinging on a heated wall. Int J Heat Mass Transf 74:101–112. https://doi.org/10.1016/j.ijheatmasstransfer.2014.02.072

Kalt PAM, Birzer CH, Nathan GJ (2007) Corrections to facilitate planar imaging of particle concentration in particle-laden flows using Mie scattering, Part 1: collimated laser sheets. Appl Opt 46:5823–5834. https://doi.org/10.1364/AO.46.005823

Koban W, Koch JD, Hanson RK, Schulz C (2004) Absorption and fluorescence of toluene vapor at elevated temperatures. Phys Chem Chem Phys 6:2940–2945. https://doi.org/10.1039/B400997E

Koban W, Koch JD, Hanson RK, Schulz C (2005) Oxygen quenching of toluene fluorescence at elevated temperatures. Appl Phys B 80:777–784. https://doi.org/10.1007/s00340-005-1769-6

Kueh KCY, Lau TCW, Nathan GJ, Alwahabi ZT (2017) Single-shot planar temperature imaging of radiatively heated fluidized particles. Opt Express 25:28764–28775. https://doi.org/10.1364/OE.25.028764

Kueh KCY, Lau TCW, Nathan GJ, Alwahabi ZT (2018) Non-intrusive temperature measurement of particles in a fluidised bed heated by well-characterised radiation. Int J Multiph Flow 100:186–195. https://doi.org/10.1016/j.ijmultiphaseflow.2017.12.017

Lau TCW, Frank JH, Nathan GJ (2019) Resolving the three-dimensional structure of particles that are aerodynamically clustered by a turbulent flow. Phys Fluids 31:071702. https://doi.org/10.1063/1.5110323

Lau TCW, Nathan GJ (2014) Influence of Stokes number on the velocity and concentration distributions in particle-laden jets. J Fluid Mech 757:432–457. https://doi.org/10.1017/jfm.2014.496

Lau TCW, Nathan GJ (2016) The effect of Stokes number on particle velocity and concentration distributions in a well-characterised,

turbulent, co-flowing two-phase jet. J Fluid Mech 809:72–110. https://doi.org/10.1017/jfm.2016.666

Lewis EW, Lau TCW, Sun Z, Alwahabi ZT, Nathan GJ (2020) Luminescence interference to two-colour toluene laser-induced fluorescence thermometry in a particle-laden flow. Exp Fluids 61:101. https://doi.org/10.1007/s00348-020-2942-8

Mi J, Nobes DS, Nathan GJ (2001) Influence of jet exit conditions on the passive scalar field of an axisymmetric free jet. J Fluid Mech 432:91–125

Miles RB, Lempert WR, Forkey JN (2001) Laser Rayleigh scattering. Meas Sci Technol 12:R33–R51. https://doi.org/10.1088/0957-0233/12/5/201

Miller F, Koenigsdorff R (1991) Theoretical analysis of a high-temperature small-particle solar receiver. Sol Energy Mater 24:210–221. https://doi.org/10.1016/0165-1633(91)90061-O

Miller VA, Gamba M, Mungal MG, Hanson RK (2013) Single- and dual-band collection toluene PLIF thermometry in supersonic flows. Exp Fluids 54:1539. https://doi.org/10.1007/s00348-013-1539-x

Pouransari H, Mani A (2016) Effects of preferential concentration on heat transfer in particle-based solar receivers. J Sol Energy Eng 139:021008–021011. https://doi.org/10.1115/1.4035163

Schulz C, Sick V (2005) Tracer-LIF diagnostics: quantitative measurement of fuel concentration, temperature and fuel/air ratio in practical combustion systems. Prog Energy Combust Sci 31:75–121. https://doi.org/10.1016/j.pecs.2004.08.002

Semrock (2018) Individual filters. https://www.semrock.com/filters.aspx

Siegel N, Ho C, Khalsa SS, Kolb G (2010) Development and evaluation of a prototype solid particle receiver: on-sun testing and model validation. J Sol Energy Eng-Trans Asme. https://doi.org/10.1115/14001146

Tea G, Bruneaux G, Kashdan JT, Schulz C (2011) Unburned gas temperature measurements in a surrogate diesel jet via two-color toluene-LIF imaging. Proc Combust Inst 33:783–790. https://doi.org/10.1016/j.proci.2010.05.074

Tsuji Y, Morikawa Y, Tanaka T, Karimine K, Nishida S (1988) Measurement of an axisymmetric jet laden with coarse particles. Int J Multiph Flow 14:565–574. https://doi.org/10.1016/0301-9322(88)90058-4

Watanabe H, Kurose R, Komori S, Pitsch H (2008) Effects of radiation on spray flame characteristics and soot formation. Combust Flame 152:2–13. https://doi.org/10.1016/j.combustflame.2007.07.021

Zamansky R, Coletti F, Massot M, Mani A (2014) Radiation induces turbulence in particle-laden fluids. Phys Fluids 26:071701. https://doi.org/10.1063/1.4890296

Zhao W, Sun Z, Alwahabi ZT (2020) Emissivity and absorption function measurements of Al2O3 and SiC particles at elevated temperature for the utilization in concentrated solar receivers. Sol Energy 207:183–191. https://doi.org/10.1016/j.solener.2020.06.079

Authors and Affiliations

Elliott W. Lewis[1,3] · **Timothy C. W. Lau**[3,4] · **Zhiwei Sun**[1,3] · **Zeyad T. Alwahabi**[2,3] · **Graham J. Nathan**[1,3]

1. School of Mechanical Engineering, University of Adelaide, Adelaide, Australia

2. School of Chemical Engineering and Advanced Materials, University of Adelaide, Adelaide, Australia

3. Centre for Energy Technology, University of Adelaide, Adelaide, Australia

4. UniSA STEM, University of South Australia, Adelaide, Australia